Materials & Design 251 (2025) 113672

Contents lists available at ScienceDirect

Materials & Design

journal homepage: www.elsevier.com/locate/matdes

Micro-arranged ZnO particles and conductive fillers in PCL composites for enhanced piezoelectric and dielectric properties in bone tissue engineering applications

Francisco Fernández-Gil [a,b,c,*], Felipe Olate-Moya [c,g,h], José Ricardo Aguilar-Cosme [d,e], Javier García-Molleja [f], Juan Pedro Fernández-Blázquez [f], Sarah Cartmell [d,e], Humberto Palza [a,c,**]

[a] Departamento de Ingeniería Química, Biotecnología y Materiales, Facultad de Ciencias Físicas y Matemáticas, Universidad de Chile, Santiago 8320000, Chile
[b] Departamento de Ingeniería Mecánica, Facultad de Ingeniería y Ciencias, Universidad de La Frontera, Temuco 4780000, Chile
[c] IMPACT, Center of Intervention Medicine for Precision and Advanced Cellular Therapy, Las Condes 7820000, Chile
[d] The Henry Royce Institute, Royce Hub Building, The University of Manchester, Manchester M1 7JA, UK
[e] Department of Materials, Faculty of Science and Engineering, The University of Manchester, Manchester M13 9PL, UK
[f] IMDEA Materials Institute, C/ Eric Kandel, 2, Parque Científico y Tecnológico Tecnogetafe, Getafe 28906, Spain
[g] Centro de Investigaciones Nucleares para Aplicaciones en Salud y Biomedicina, Comisión Chilena de Energía Nuclear, Las Condes 7600713, Chile
[h] Centro de Investigación e Innovación Biomédica, Facultad de Medicina, Universidad de Los Andes, Las Condes 7620001, Chile

ARTICLE INFO

Keywords:
Piezoelectricity
Scaffold
3D-printing
Interfacial polarization
Ultrasound
Particle alignment

ABSTRACT

Piezoelectric polymers are promising for replicating bone tissue's piezoelectric properties. Typically, non-piezoelectric biopolymers are combined with piezoelectric particles, but this yields low piezoelectric output. We addressed this by aligning piezoelectric zinc oxide (ZnO) micro-rods in 3D-printed polycaprolactone (PCL) scaffolds and adding conductive particles like thermally reduced graphene oxide (TrGO). Our findings revealed that controlled particle alignment in PCL/ZnO composites significantly enhanced dielectric properties. TrGO further improved these properties by creating conductive pathways and micro-capacitor networks by apparent polarization due to electron displacement, promoting Maxwell-Wagner-Sillars effect. This design strategy significantly increased dielectric and piezoelectric performance, achieving values akin to bone tissue. TrGO also boosted the piezoelectric response, with maximum voltage generation of 696 ± 52 and 142 ± 9 mV during direct contact mechanical pressure by a linear actuator and remote mechanical pressure induced by ultrasound waves, respectively. The 3D-printed composites demonstrated bioactivity for MC3T3-E1, enhanced ALP activity, improved cell adhesion, migration, and extracellular matrix formation under remote ultrasound stimulation, underscoring the potential of these novel ternary composites for bone tissue engineering.

1. Introduction

Annually, approximately 2.2 million surgical grafting procedures are performed worldwide, with autografts remaining the gold standard despite challenges such as donor-site morbidity [1]. To address these limitations, synthetic scaffolds have emerged as viable alternatives, emphasizing their biocompatibility, mechanical properties, and bioactivity in supporting osteoblast proliferation and bone regeneration [2,3]. Among these, smart biomaterials that respond to stimuli including mechanical stress show significant promise [4,5]. Inspired by the piezoelectric properties of bone, biomimetic scaffolds incorporating piezoelectricity are gaining attention for their ability to generate electrical signals under mechanical stimuli, enhancing cellular responses such as calcium signaling and growth factor activation [6–9]. Among various types of materials, piezoelectric polymers are particularly attractive for scaffold design because of their processability, tunable degradation, and favorable mechanical properties [10,11]. These polymers include bulk materials, such as polyvinylidene fluoride (PVDF) and poly L-lactic acid (PLLA), piezoelectric polymer composites (PPCs), and voided charged polymers [12]. PPCs combine biocompatible polymer

* Corresponding author at: Francisco Salazar 1145, 4811230 Temuco, Chile.
** Corresponding author at: Av. Beauchef 851, 8370456 Santiago, Chile.
E-mail addresses: francisco.fernandez@ufrontera.cl (F. Fernández-Gil), hpalza@ing.uchile.cl (H. Palza).

https://doi.org/10.1016/j.matdes.2025.113672
Received 13 December 2024; Received in revised form 17 January 2025; Accepted 24 January 2025
Available online 25 January 2025

matrices with piezoelectric particles such as barium titanate ($BaTiO_3$) and zinc oxide (ZnO), offering flexibility and enhanced bioactivity [13,14]. However, optimizing PPC performance requires careful consideration of the particle type, alignment, dielectric properties, and matrix conductivity [15–18].

Strategies for aligning piezoelectric particles dipoles within PPCs are critical to enhance their functionality. Traditional methods, such as poling, mechanical stretching, thermal annealing, and electrospinning, are effective for orienting dipoles in ferroelectric fillers, but may impose limitations on scaffold geometry, require high temperatures, or compromise structural integrity [6,19]. For non-ferroelectric fillers, dipole alignment relies on physical techniques such as dielectrophoresis [20], two-photon polymerization (TPP) [21], and uniaxial strain assembly [22]. For example, ZnO microparticles aligned in a polydimethylsiloxane (PDMS) matrix using dielectrophoresis demonstrated improved piezoelectric properties [23], whereas TPP-enhanced ZnO nanowire alignment enabled better electron transport for sensor applications [24]. Despite these advances, current methods often have limitations, including matrix compatibility, high costs, and complex setups [25,26]. To address these challenges, 3D-printing extrusion has emerged as a promising alternative for particle alignment, offering simplicity, scalability, and compatibility with high aspect ratio particles. This method avoids the high temperatures or voltages of other techniques, while allowing complex scaffold geometries [26,27]. However, its application in non-ferroelectric PPCs remains underexplored, representing a novel and practical approach for enhancing piezoelectric properties.

Incorporating piezoelectric fillers into PPCs enhances their piezoelectric response beyond the rule of mixtures by increasing the material's permittivity and piezoelectric constant (d_{33}). This constant, which measures electric polarization induced by mechanical stress, is explained by: $d_{33} = k\sqrt{s^*\varepsilon_r{}^*\varepsilon_0}$, where k is the electromechanical coupling factor, s is mechanical compliance, ε_r is relative permittivity, and ε_0 is vacuum permittivity [18]. The enhancement is often due to Maxwell-Wagner-Sillars (MWS) interfacial polarization, caused by charge accumulation at the matrix-filler interfaces due to differing dielectric properties and relaxation times, thus improving dielectric properties and piezoelectric output [28]. While the introduction of porosity and surface chemical modification of piezoelectric particles represents novel techniques to enhance dielectric and piezoelectric properties in PPCs, these methods are challenging to implement and introduce additional manufacturing steps that compromise their scalability. Consequently, alternative strategies warrant consideration. A viable approach to augment dielectric and piezoelectric properties involves the incorporation of a third conductive phase into the PPC, which enhances interfacial charge accumulation due to increased conductivity mismatches and electron migration, thereby forming a micro-capacitor network.[29,30]. For instance, Jin et al. developed ternary composites of polyamide 11, $BaTiO_3$, and graphene via ultrasonic coating and selective laser sintering (SLS), achieving superior dielectric permittivity and piezoelectric properties [31]. Similarly, Qi et al. reported significant dielectric property improvements and a 23.5 % increase in d_{33} in polyamide 11 composites with $BaTiO_3$ and carbon nanotubes (CNT), highlighting the synergistic effect of conductive and piezoelectric fillers [32]. Additionally, current PPCs are limited by the nonconductive nature of their matrices, hindering efficient electric charge transfer generated by piezoelectric fillers under mechanical deformation [33]. Adding an electrically conductive phase can enhance charge distribution by collecting piezoelectric charges from particles during deformation, thereby improving the overall piezoelectric response [34,35]. Conductive particles also enhance the bioactivity of composite scaffolds in tissue engineering [36]. For example, a ternary composite with 5 wt% PANI nanoparticles added to a PCL matrix containing 40 wt% $BaTiO_3$ increased voltage generation ~6-fold and significantly boosted MG-63 cell growth and proliferation, highlighting the multifunctional advantages of incorporating conductive phases into piezoelectric scaffolds [37].

This study investigates a novel PPC design incorporating thermally reduced graphene oxide (TrGO) into a biodegradable polycaprolactone (PCL) matrix with piezoelectric ZnO micro-rods possessing osteogenic properties. Utilizing 3D-printing to align ZnO particles and create TrGO conductive networks, the composite showed improved dielectric, piezoelectric, and bioactive properties. Parameters such as permittivity, dielectric losses, and voltage generation were assessed, alongside cell adhesion and proliferation in MC3T3-E1 preosteoblasts under remote ultrasound stimulation. This hierarchical design highlights the potential of multifunctional, remotely activated piezoelectric scaffolds for bone tissue engineering.

2. Material and methods

2.1. Materials

The following materials were purchased and used as received: graphite powder, potassium permanganate, sodium nitrate, sulfuric acid, hydrogen peroxide, ethanol, hydrochloric acid, hexahydrate zinc nitrate, N,N-dimethylformamide, and polycaprolactone (Mn = 80.000) were sourced from Sigma-Aldrich or Merck, Millipore (USA). Hexamethylenetetramine (HMT) (99 %) and polydimethylsiloxane were obtained from Thermo Fisher Scientific (USA) and Smooth-On (USA), respectively. Phospate-buffered saline (PBS) and Dulbecco's Modified Eagle's Medium (DMEM) were purchased from Sigma-Aldrich (USA), while fetal bovine serum (FBS) and penicillin–streptomycin were sourced from Gibco (Australia). Ascorbic acid, β-glycerophosphate, and dexamethasone were acquired from Sigma-Aldrich (USA). For bioassays, lysis buffer was purchased from Macherey Nagel Bioanalysis (Germany), the QuantiFluor dsDNA assay kit from Promega (UK), and the alkaline phosphatase (ALP) kit from AAT Bioquest (USA). DAPI (4′,6-diamidino-2-phenylindole) was obtained from GeneTex (USA), and Alexa Fluor 568-conjugated phalloidin, 4 % paraformaldehyde, and Triton X-100 were purchased from Thermo Fisher Scientific (USA). All materials were used without further purification. Thermal reduced graphene oxide (TrGO) was prepared from graphene oxide (GO) synthesized via a modified Hummer's method as reported previously [36].

2.2. Zinc oxide micro-rods synthesis

ZnO micro-rods were synthesized using a modified low hydrothermal method from Chandraiahgari et al. [38]. Initially, 2.9 g of hexahydrate zinc nitrate were mixed with 300 mL deionized water and stirred magnetically for 15 min. Then, 100 mL of deionized water containing 1.4 g of HMT was added dropwise at room temperature, followed by 30 min of stirring. The mixture was then heated at 90 °C for 4.5 h. After cooling overnight to room temperature, the precipitate was ultrasonically dispersed for 5 min to dislodge any ZnO adhered to the vessel walls, producing a white solution. This solution was centrifuged at 8,000 RPM for 10 min to remove excess water and impurities and washed multiple times with absolute ethanol. The particles were dried overnight at 80 °C and calcined at 400 °C for two hours, yielding a white ZnO powder.

2.3. Hybrid ZnO/TrGO particle fabrication

To enhance ZnO and TrGO interaction in composites, hybrid particles were prepared matching the final PCL composite weight ratio. Initially, 11.8 g of ZnO micro-rods were dispersed in 40 % N,N-dimethylformamide solution for stability and stirred until a white dispersion formed. Based on TrGO concentration in the PCL composite, 66 mg (0.2 wt%) and 165 mg (0.5 wt%) were added and stirred for 10 min. The mixture was then sonicated with an ultrasound probe for 10 min, transferred to a preheated oven at 90 °C, and maintained for 4.5 h

until room temperature. Post-process, the mixture was resuspended in an ultrasound bath, washed with absolute ethanol by centrifugation at 8,000 RPM for 10 min, and dried overnight at 80 °C, yielding a gray ZnO/TrGO powder.

2.4. Melt mixed composite fabrication

PCL composites were prepared by melt mixing with a Bravender Plastic Corder (Germany) preheated to 90 °C. Pre-dried PCL pellets (30 °C for one hour) were added to the chamber and mixed at 25 RPM until fully melted. ZnO, TrGO, and ZnO/TrGO particles (per Table S1) were then added, mixed at 100 RPM for 10 min, and flattened into discs using a hydraulic press. The resulting composites were cut into small pellets. For random particle distribution, the solvent casting method was used: PCL was dissolved in chloroform, ZnO, TrGO, and ZnO/TrGO particles (per Table S1) were added, and the mixture was stirred magnetically for 30 min. The viscous solution was then poured into glass Petri dishes, covered with aluminum foil, and allowed to evaporate at room temperature.

2.5. Filament fabrication and 3D-printing

The "3devo Filament Maker" (3devo, USA) produced filaments by inserting small composite cut pellets into the chamber, extruding them at 1.75 mm diameter following the temperature parameters in Table S2, with the screw rotating at 2 RPM. The filaments were 3D-printed using a Prusa i3 MKs+ printer (Prusa, Czech Republic) at an extrusion speed of 1 mm/s, nozzle temperature of 200 °C, bed temperature of 30 °C, and a flow rate of 100 %. Scaffolds and characterization probes were designed in FreeCAD, and G-codes generated with Ultimaker Cura (Cura, Netherlands). Glue was applied to the print bed before each print and removed with deionized water.

2.6. Materials characterization

The synthesized and fabricated particles and materials were characterized utilizing techniques such as X-ray diffraction (XRD), scanning electron microscopy (SEM), Fourier transform infrared spectroscopy (FT-IR), thermogravimetric analysis (TGA), Raman spectroscopy, differential scanning calorimetry (DSC), micro-CT, wide-angle X-ray scattering, impedance analysis, Berlincourt Piezo meter d_{33} and electrical generation. Mammalian cell culture was conducted using MC3T3-E1 preosteoblast cells, while metabolic activity, dsDNA extraction, ALP activity and confocal fluorescence microscopy were performed to assess the bioactivity of 3D-printed scaffolds under ultrasound (US) conditions. Sketch of cell culture protocol is presented as Fig. S1. Detailed methodologies are provided in the Supplementary Materials.

2.7. Statistical analysis

The results are presented as mean ± standard deviation. To determine statistical significance between groups, analysis of variance (ANOVA) and Tukey's post-test were conducted using OriginPro 8.6 (Origin-Lab) or Prism 10 (GraphPad).

3. Results and discussion

3.1. Particle characterization

The XRD analysis (Fig. S2a) confirmed the hexagonal wurtzite structure of ZnO with characteristic peaks at 2θ = 31.7°, 34.4°, and 36.2° (planes (1 0 0), (0 0 2), and (1 0 1)), and an average crystallite size (D) of ~54 nm calculated using the Debye-Scherrer equation, stating that $D = \frac{0.89*\lambda}{\beta^{*}cos\theta}$, where λ is the wavelength of the X-ray source, β is the full width at half maximum, and θ is the Bragg's diffraction angle. This D value seems to be larger than other ZnO synthesized particles [39,40], which can be related to a low-pressure synthesis and higher time of reaction. Nonetheless, higher values of D are capable to allocate a major number of internal dipoles, thus increasing the dielectric properties of ZnO [41]. FT-IR spectra (Fig. S2b) showed peaks at 3.300 cm^{-1} (O-H bending), 2.950 cm^{-1} (HMT precursor), and 420 cm^{-1} (Zn-O bond). TGA results (Fig. S2c) demonstrated high thermal stability of ZnO. For carbon materials, XRD patterns (Fig. S2d) revealed graphite's sharp (0 0 2) peak at 2θ = 26.4° with an interlaminar distance of 3.3 Å. Oxidation shifted this peak to 2θ = 12.6°, increasing interlaminar distance to 6.9 Å, confirming GO formation with increased functionalization. After thermal reduction, TrGO showed partial recovery of the graphitic structure with a peak at 2θ = 25.2°, meaning a reduction in interlaminar distance to 3.5 Å, reduced functional groups, and a disordered arrangement. FT-IR spectra (Fig. S2e) confirmed GO's oxidation with peaks for O–H (3.2000 cm^{-1}), C═O (1.715 cm^{-1}), COOH, and C–O–C, which diminished in TrGO. TGA (Fig. S2f) showed GO's multi-step degradation up to 500 °C, while TrGO had a single high-temperature process. Raman spectroscopy (Fig. S3) further confirmed TrGO's reduction, showing an increased I_D/I_G ratio and broader full-width at half maximum (FWHM), indicating more defects and fragmented sp^2 regions [42,43]. Fig. S2g shows SEM images of ZnO's presenting a hexagonal micro-rod morphology with an average diameter and length of 0.91 μm and 6.6 μm, respectively. The resulting morphology can be explained by HMT building block property, acting as a chelating agent forming stable multidentate ligands that promote growth in single dimensions [44]. Fig. S2h and i presents TrGO's porous structure due to gas release during reduction, and the hybrid TrGO/ZnO preserving both morphologies, respectively.

3.2. 3D-printed composites

XRD analysis of the 3D-printed composites (Fig. S4) indicates that increasing particle concentration from 5 wt% to 30 wt% enhances the intensity of ZnO crystalline peaks while reducing PCL characteristic peaks, implying decreased polymer chain order. Previous studies suggest nanoparticle incorporation might increase polymer chain alignment by disentangling molecular chains [45]; however, XRD indicates the opposite effect here. Though particle dimensions might influence this, filler concentrations are more critical in determining polymer chain alignment [46], thus the reduced PCL crystalline peaks are attributed to higher ZnO concentration. Compared to ZnO powder, the 3D-printed parts show an inversion of the (1 0 0)/(1 0 1) ratio in the wurtzite planes, signaling preferential crystal orientation, and an increased peak intensity of the (1 1 0) plane, parallel to the ZnO crystal's c-axis. These suggest micro-rods are aligned longitudinally in the 3D-printed parts. For ternary composites, XRD shows this alignment with the (1 1 0) plane from ZnO, albeit slightly disrupted by TrGO incorporation.

Table S3 presents the DSC parameters for each 3D-printed composite. PCL exhibits a crystallinity of 52.9 % and a fusion temperature of 58.1 °C during the second heating, and a crystallization temperature of 33.5 °C during cooling, consistent with previous reports [47]. The addition of ZnO micro-rods enhances polymer crystallinity, reaching 61.5 % for composites with 15 wt% ZnO. This increased crystallinity is attributed to particle nucleation and improved polymer chain alignment within the PCL matrix [48]. In ternary composites, higher TrGO concentrations reduce the overall crystallization degree due to steric obstruction, which inhibits crystal formation, and particle aggregation during chain crystallization [49]. ZnO incorporation raises the fusion temperature of PCL from 58.1 °C to 63.1 °C in 10 wt% ZnO composites, likely due to thicker crystalline sheets formed from additional nucleation sites, enhancing crystallinity [50]. Conversely, TrGO reduces fusion temperatures in ternary composites compared to pure PCL, due to melt mixing and particle aggregation affecting polymer chain compaction.

Fig. 1 presents SEM images of 3D-printed filaments. The pure polymer (Fig. 1a) and the composite with 10 wt% ZnO (Fig. 1b) have smooth surfaces, indicating minimal roughness impact from ZnO incorporation. The ternary composite with 30 wt% ZnO and 0.5 wt% TrGO (Fig. 1c) exhibits a wavier surface, attributed to the higher particle count. Electron backscattering SEM images reveal no particles in pure PCL (Fig. 1d), but isolated ZnO micro-rods appear in PCL with 10 wt% ZnO (Fig. 1e) and 30 wt% ZnO with 0.5 wt% TrGO (Fig. 1f), confirmed by EDS (Figs. S5 and S6). Both binary and ternary composites show significant longitudinal alignment of ZnO particles induced by extrusion, due to the anisotropic geometry of ZnO micro-rods and shear forces during 3D extrusion. This effect results from the combination of the anisotropic geometry of the ZnO micro-rods and the high shear forces induced on the flow during the 3D extrusion, where tangential forces will apply a torque to spin the particles while a translational force will move the particle in the flow direction [51]. Fig. 1g displays a smooth PCL cross-section after fracture, while PCL with 10 wt% ZnO (Fig. 1h) and 30 wt% ZnO with 0.5 wt% TrGO (Fig. 1i) shows micro-rods and voids from cryofracture. These cross-sections also exhibit preferential particle alignment, in-plane direction, consistent with surface images and extrusion shear stress effects (Fig. S7).

Figs. S8a and b display micro-CT images of a filament before and after 3D printing, respectively, for the sample with 30 wt% ZnO. The sagittal and coronal images confirm that in both cases, the micro-rods show preferential directionality at lower zenith angles, as depicted in the particle fraction graph. This longitudinal directionality is consistent with SEM images of the 3D-printed grids and X-ray diffractions. Notably, the 3D-printed parts exhibit less particle alignment than the filaments. Parameters such as line width, layer height, flow velocity, and nozzle properties significantly influence particle and short fiber alignment during extrusion [52]. In this case, this phenomenon is primarily due to the different nozzle diameters used in fabricating the filaments and 3D-printed parts. Larger nozzles can produce larger jets, potentially aligning particles more effectively due to the increased cross-sectional area for particle interaction [53]. Additionally, the drawing ratio used in filament production contributes to the higher alignment in the original filament. This tendency is confirmed by WAXS patterns of PCL shown in Fig. 2, with 5 wt% and 30 wt% ZnO in three configurations: a pressed film (composite), and filaments before and after 3D printing. The internal meridians indicate that the as-prepared composites show preferential alignment of polymer crystal lamellae and chains, likely due to high compression stress during melt pressing. The external meridians, associated with ZnO micro-rod morphology, reveal poor or non-preferential particle alignment, consistent with SEM images (Fig. S9). For filaments, 5 wt% ZnO shows higher alignment in preferred directions, indicated by anisotropic external meridians. At 30 wt% ZnO, a broader distribution suggests lower alignment due to higher particle concentration [54]. This reduced alignment might be due to longer alignment times needed for particles to accommodate, as stronger steric interactions occur, as noted by Hausmann et al. [55]. Polymer chains lose alignment at low particle concentrations but regain it at higher filler concentrations, potentially due to confinement effects by the high concentration of micro-rods acting as channels [56]. WAXS patterns of 3D-printed samples show decreased alignment of particles and polymer chains compared to filaments, akin to micro-CT findings. This reduced alignment in 3D parts may result from varying extrusion speeds, leading

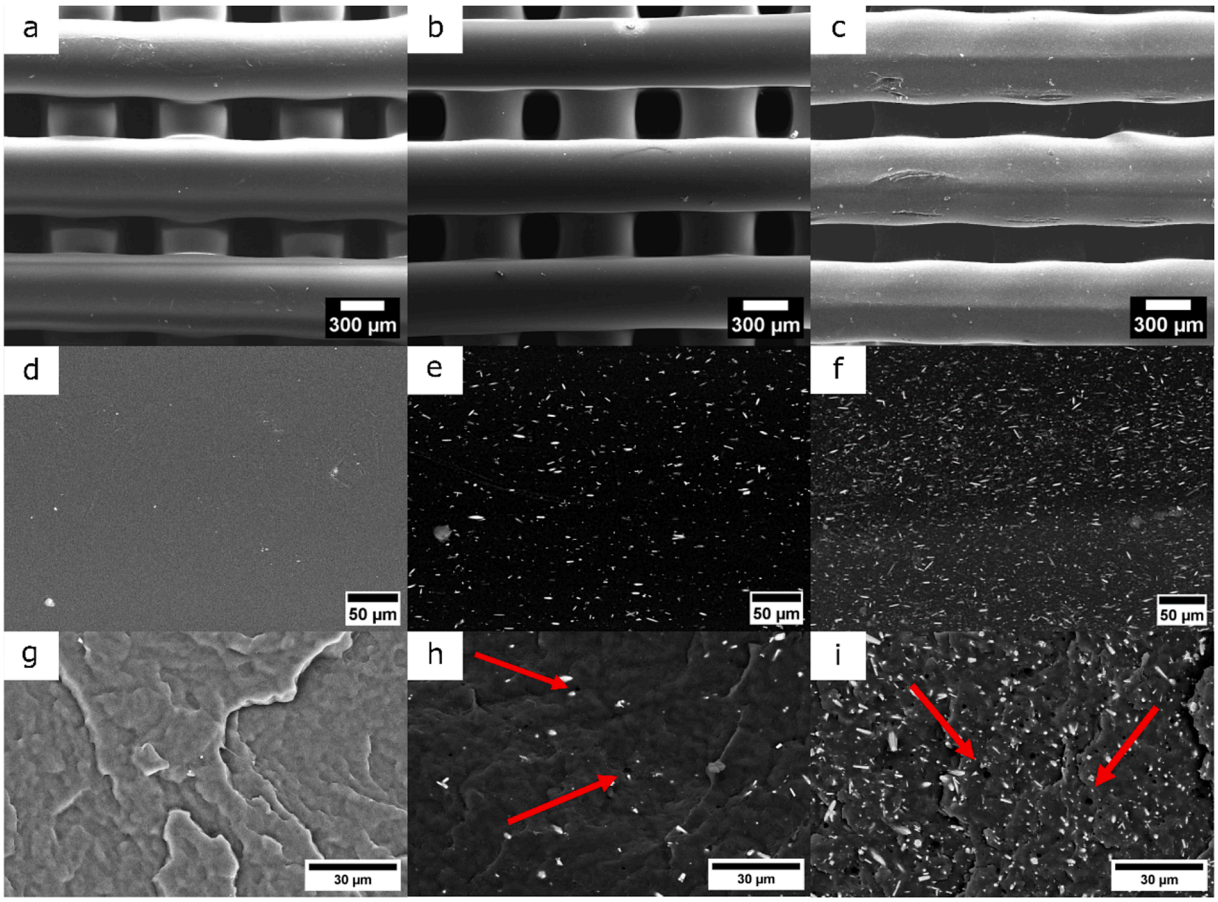

Fig. 1. SEM images of a) PCL, b) PCL with 10 wt% ZnO, and c) PCL with 30 wt% ZnO – 0.5 wt% TrGO of 3D-printed grids. SEM images with electron backscattering of d) PCL, e) PCL with 10 wt% ZnO, and c) PCL with 30 wt% ZnO – 0.5 wt% TrGO of 3D-printed surfaces. SEM images with electron backscattering of 3D-printed cross sections of g) PCL, h) PCL with 10 wt% ZnO, and i) PCL with 30 wt% ZnO – 0.5 wt%. Red arrows in Fig. 2h and i indicate holes where particles were previously allocated.

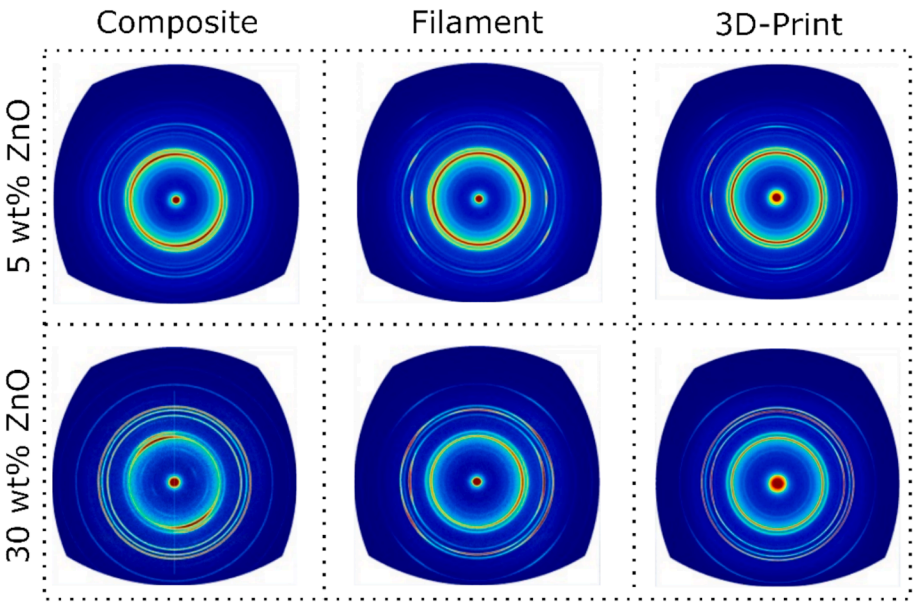

Fig. 2. Measured WAXS patterns of composites, filaments, and 3D-printed parts made of PCL with 5 and 30 wt% ZnO.

to more turbulent regimes and non-uniform shear stress distribution. However, further rheological investigations are required to confirm these observations.

3.3. Mechanical properties

Fig. 3a and b present the tensile elastic moduli and strength of 3D-printed parts, revealing that composites showed increases of 60.7 %, 105.7 %, 72.6 %, and 54.6 % in elastic modulus and 61.3 %, 116.5 %,

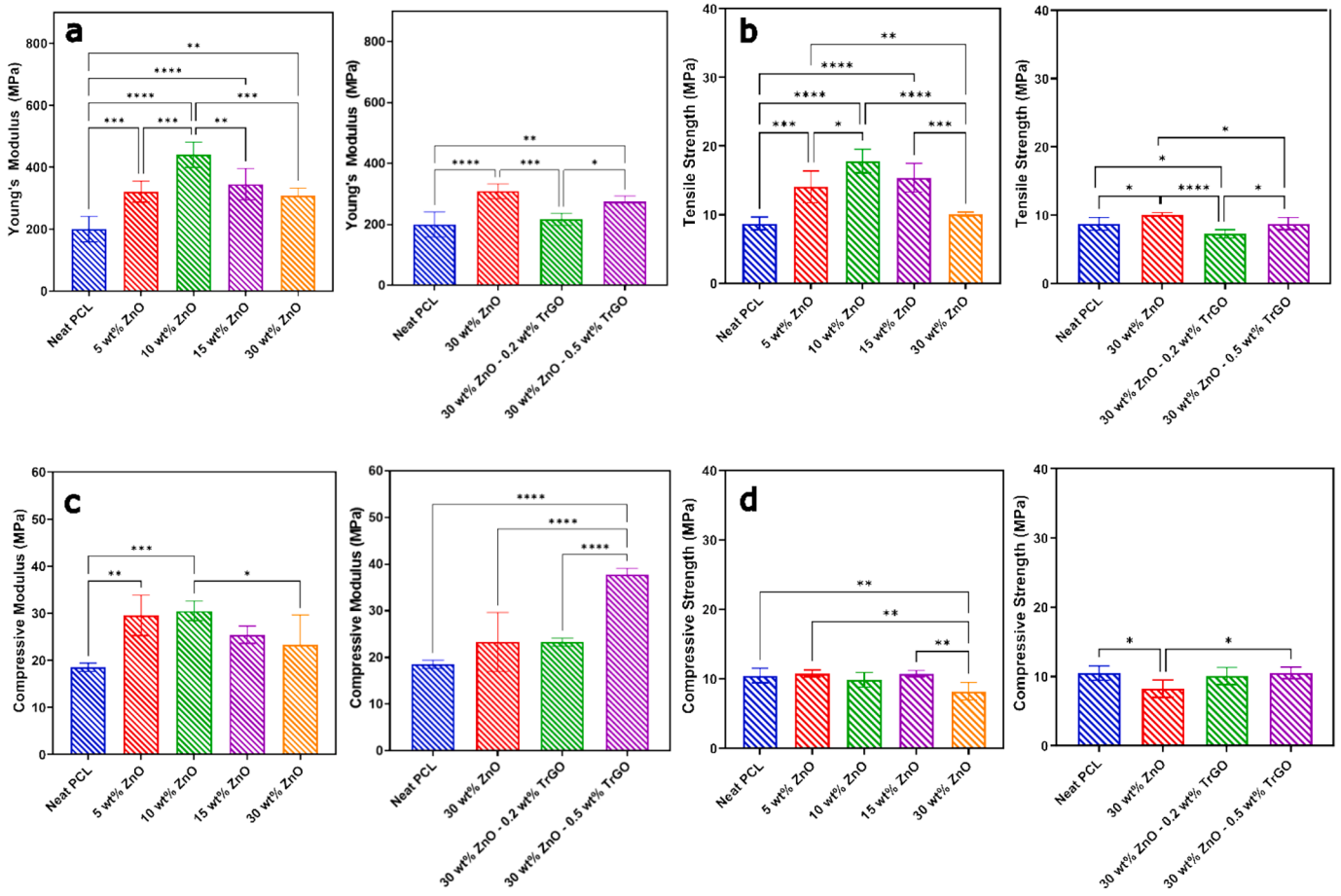

Fig. 3. Mechanical properties of 3D-printed composites, showing a) Young's modulus , b) tensile strength, c) compressive modulus, and d) compressive strength obtained trough uniaxial tensile and compressive tests. ns: not significant, *: $p < 0.05$, **: $p < 0.01$, ***: $p < 0.001$, ****: $p < 0.0001$.

76.6 %, and 15.8 % in tensile strength at ZnO concentrations of 5, 10, 15, and 30 wt%, respectively. The improvements in mechanical properties are due to the stiffness filler's reinforcement effect, its high aspect ratio (~7.25), preferential alignment along the longitudinal direction of the 3D-printed probes, and good dispersion. However, higher concentrations lead to particle agglomeration, reducing the reinforcement effect due to weak electrostatic interactions. Fig. S10 shows that oriented particles resulted in a 2.2-fold increase in Young's Modulus and a 2.0-fold increase in tensile strength of Neat PCL compared to non-oriented particles, which slightly reduced the elastic modulus and achieved only a 1.5-fold increase in tensile strength. These results suggest that particle alignment from 3D-printing enhances stress distribution at higher filler concentrations. Additionally, the 3D-printed composites exhibited significant stiffness (199.8 MPa to 440.7 MPa) and tensile strength (7.27 MPa to 17.80 MPa), making them suitable as bone tissue scaffolds, as the osteoid matrix has an elastic modulus ranging from 0.024 MPa to 20 GPa, and trabecular bone ranges from 20 to 500 MPa [57]. Regarding the mechanical properties under compression, as shown in Fig. 3c and 3d for compressive modulus and strength, the addition of ZnO to the PCL matrix increased the compressive modulus by 59.2 %, 64.4 %, 37.1 %, and 25.4 % for ZnO concentrations of 5, 10, 15, and 30 wt%, respectively, paralleling results from tensile tests. While ternary composites increased the compressive modulus by up to 103.5 %, showing a synergistic effect on compression stiffness without significantly altering compressive strength.

3.4. Dielectric properties

Fig. 4a and b illustrate the dielectric permittivities of the as-prepared (random particle distribution) and 3D-printed (aligned particle distribution) composites. These composites displayed significantly higher permittivity than pure polymer, especially at low frequencies, though this effect diminishes at higher frequencies. The low-frequency permittivity increase is attributed to the MWS effect, where dipole alignment in the electric field direction leads to charge accumulation at polymer/particle interfaces, creating local microcapacitors. At higher frequencies, dipoles reorient less effectively, decreasing their polarization capacity and thus the relative permittivity. The permittivities are consequently linked to the number of microcapacitors between the matrix and particles [58]. Notably, the 3D-printed parts exhibited higher relative permittivities than the as-prepared PCL composites due to particle alignment. Aligned ZnO micro-rods increase the total dipole moment, enhancing relative permittivity, although at high concentrations, particle agglomeration reduces this effect. For ternary composites, the conductive particle slightly increases the permittivity of 3D-printed samples at low frequencies, whereas in as-prepared composites, it either decreases or remains unchanged due to high particle concentration and random filler distribution, which hinder polarization. The enhanced dielectric permittivity due to TrGO particles is mainly attributed to interfacial polarization, but Li et al. suggest it results from electron migration near conductive particles forming dipoles. When particles cluster, electron migration establishes dipoles that enhance dielectric properties [29]. Dielectric losses were also measured (Fig. S11a and b), showing that the particles shift the loss peak, especially for ternary samples. In 3D-printed composites, a loss peak appears at 10 wt% ZnO due to dipole relaxation, while in as-prepared composites, the peak is absent. Particle alignment in 3D-printing reduces relaxation times but decreases at higher ZnO content, lowering dipole moment and charge

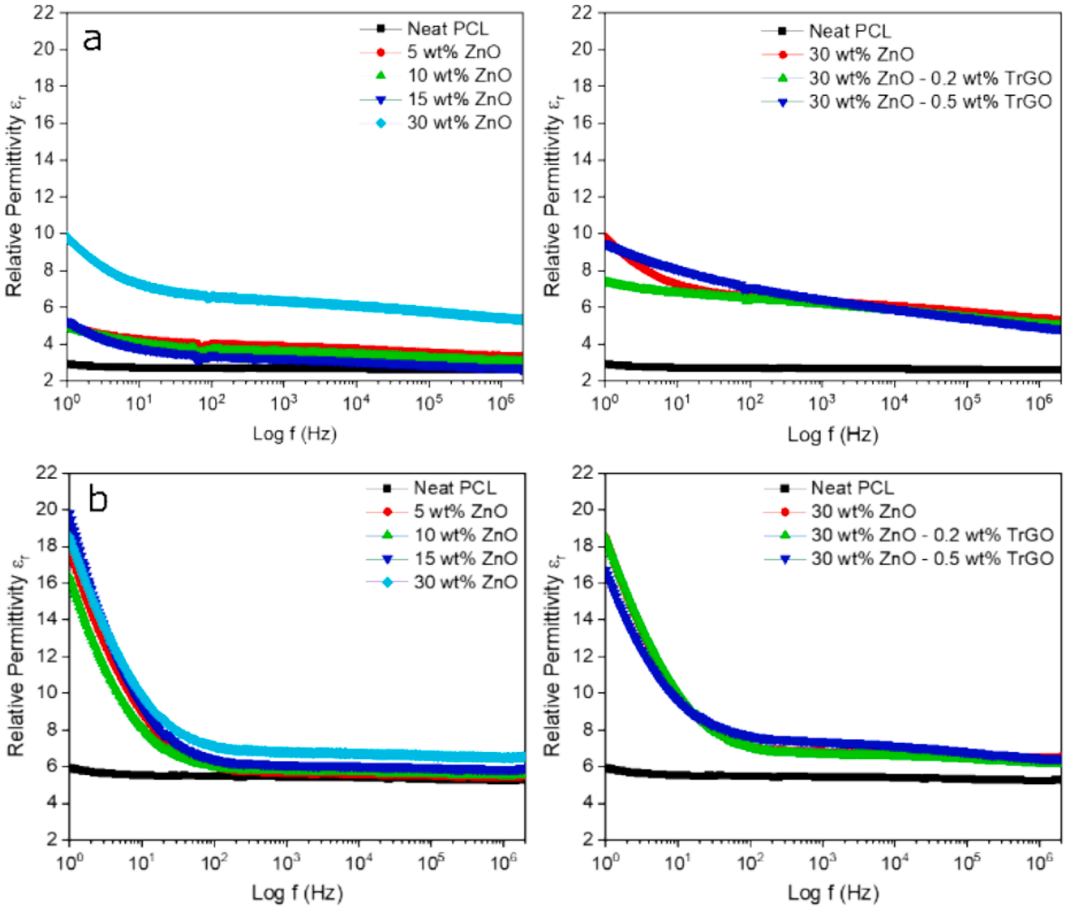

Fig. 4. Relative permittivity of a) as-prepared composites with random particle orientation and b) 3D-printed parts with aligned particles. The graphs on the left correspond to the comparison between binary composites, whereas the graphs on the right correspond to the comparison between ternary composites.

mobility. Ternary composites further increase losses due to conductivity differences between components, causing current leakage and higher dipole moments.

3.5. Piezoelectric properties

PPCs' piezoelectric properties are evaluated using the piezoelectric charge constant, d_{33}, indicating electrical charge and polarization induced by mechanical load. Fig. S12a and b depict d_{33} for composites with randomized and aligned micro-rods, respectively. In non-aligned samples, a detectable piezoelectric signal appears only with 30 wt% ZnO, yielding about 0.1 pC/N, and increases to 0.2 pC/N with 0.5 wt% TrGO. Aligned 3D-printed composites show improved performance starting at 10 wt% ZnO and reach approximately 0.3 pC/N with 30 wt% ZnO. The alignment also enhances the effect of the conductive filler, achieving 1.1 pC/N in ternary composites with 0.5 wt% TrGO. This indicates that particle alignment in 3D-printed composites enhances macroscopic piezoelectric behavior, requiring less filler. This occurs despite alignment and strain reducing interconnected networks for piezoelectric performance [59], highlighting the stronger effect of aligned dipoles facilitating charge transport along the insulating PCL matrix. The superior piezoelectric properties in ternary composites arise from electrically conductive pathways that enhance electron flow and increased dielectric permittivity due to electron migration around particles inducing additional polarization. Fig. S13 shows that the permittivity at 110 Hz, the frequency at which d_{33} was measured, follows a similar pattern to d_{33}, reinforcing that dielectric properties enhance piezoelectric output. Further studies are needed to fully understand these composites' piezoelectric properties. While the Berlincourt meter used in this study has been widely applied to measure the piezoelectric constant of various polymeric composites [60–62], future research should include piezoresponse force microscopy (PFM) to explore

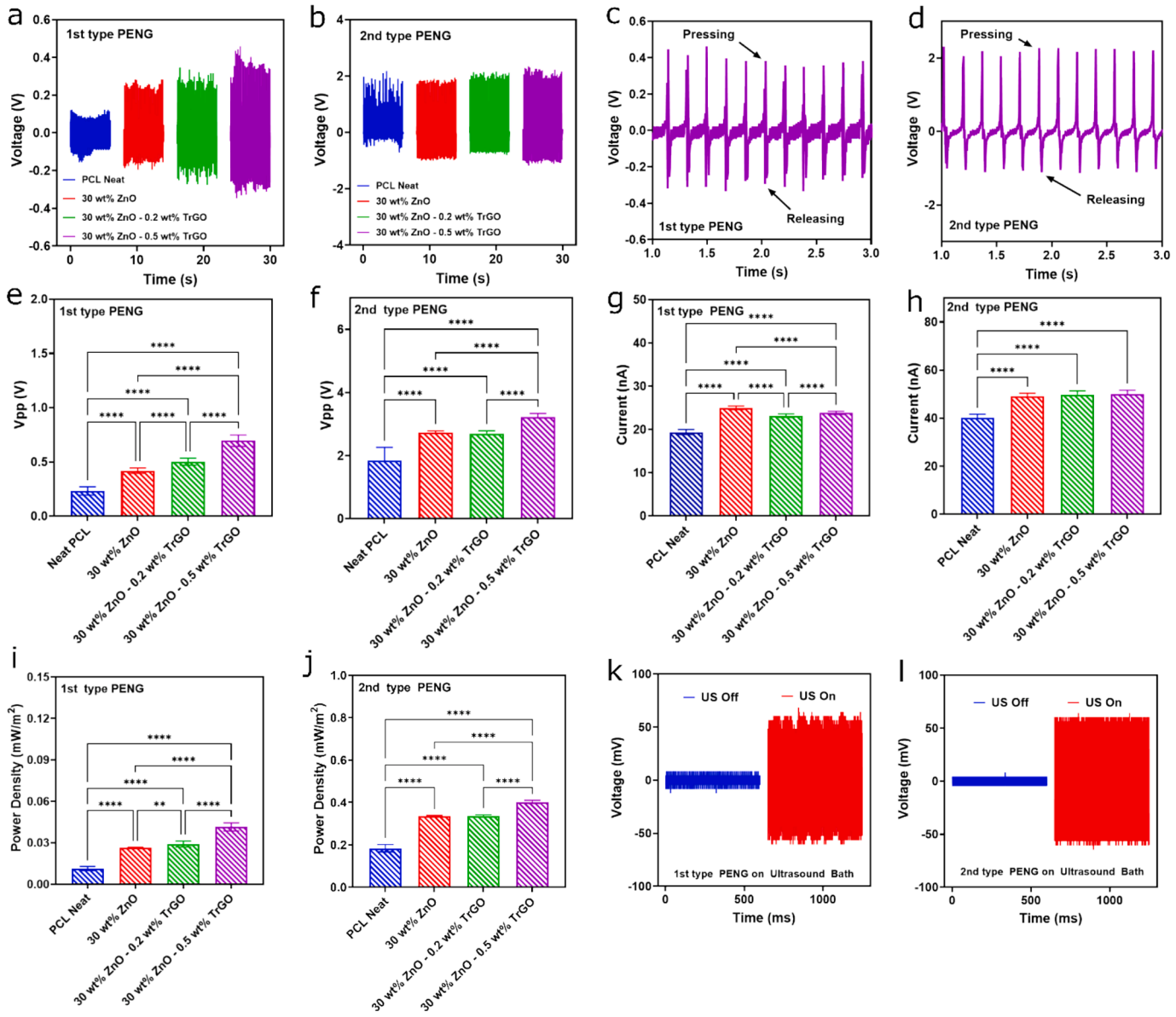

Fig. 5. Piezoelectric output of PENGs using 3D-printed composites with aligned particles. Voltage output of a) first-type PENGs and b) second-type PENGs. Voltage generation dynamic from c) first-type PENG and d) second-type PENG of PCL composite with 30 wt% ZnO – 0.5 wt% TrGO. Peak-to-peak voltages of e) first-type PENGs and f) second-type PENGs. Current generation of g) first-type PENGs and h) second-type PENGs. Power density generated by i) first-type PENGs and j) second-type PENGs. Voltage generation under ultrasound waves in an ultrasound bath showing the off and on condition in k) first-type PENGs and l) second-type PENGs. ns: not significant, *: $p < 0.05$, **: $p < 0.01$, ***: $p < 0.001$, ****: $p < 0.0001$.

converse mechanisms, potentially offering deeper insights.

The performance of 3D-printed piezoelectric composites with the highest d_{33} was evaluated using two PENGs devices to analyze the triboelectric effect's contribution, often present but poorly addressed in voltage output. Fig. 5a shows the voltage output of the first PENGs type, without a PDMS outer layer to avoid extra electrical induction. Here, the neat PCL PENG generated maximum voltages of 109 ± 44 mV, increasing to 256 ± 14 mV with 30 wt% aligned ZnO micro-rods. Incorporating TrGO particles further increased the voltage to 281 ± 30 mV and 392 ± 37 mV for 0.2 wt% and 0.5 wt% TrGO concentrations, respectively. Fig. S14 shows that oriented particles doubled the voltage generation compared to random particle orientation, due to more aligned dipoles contributing to greater charge polarization in the same direction, indicating that particle alignment enhances voltage generation. The voltage generated by neat PCL, a non-piezoelectric polymer, results from triboelectric effects likely due to different surface contacts in the device inducing electrical processes during testing. For example, contact between the insulating resin block from the linear actuator's pusher and the external-insulating Kapton layer from the PENG device during mechanical stimulation causes electrons to flow from the resin to the Kapton due to their positions in the triboelectric series. When separated, opposite charges remain, creating a voltage between the materials. PCL acts as a triboelectric layer, donating electrons to the Kapton during friction from mechanical stimulation. The copper electrode in the PENG collects these triboelectric charges, explaining the generated voltage. In composites, voltage generation increases due to the piezoelectric effect, as ZnO deforms under mechanical stimulus, creating charge polarization and piezoelectric voltage added to the triboelectric voltage. While flexoelectricity, which is the induced polarization by strain gradients, generates a great contribution in voltage generation in PENGs made of polymeric matrix due to high flexibility, especially at the nanoscale, in this case the PENG deformation is restricted in the y-axis, so high macroscopic deformations are not expected, thus lowering the effects of flexoelectricity. Then, charge generation can be mainly attributed to piezoelectric phenomena in the case of binary and ternary composites. Incorporating TrGO further increases output voltage, confirming enhanced piezoelectric behavior of ternary composites, as the conductive filler provides a pathway to collect piezoelectric charges. The significance of the triboelectric effect is confirmed by results from the PENG with an extra external-insulating PDMS layer, which increases material layer interactions (Fig. 5b). Voltages significantly increase, reaching up to 1.61 ± 0.2 V for neat PCL, indicating PDMS significantly contributes to triboelectric generation. Despite the high triboelectric effect, composites with 30 wt% ZnO showed a maximum voltage of 1.78 ± 0.1 V, increasing to 2.18 ± 0.1 V for the ternary composite with 0.5 wt% TrGO due to piezoelectric contribution. Fig. 5c and d illustrate the voltage dynamics generated by both PENG types for the ternary composite. During pressing by the linear actuator, the PENG produces a positive voltage due to piezoelectric charges on deformed ZnO. When the actuator separates, a negative peak occurs due to charge repolarization [63]. The difference between the positive and negative peaks, known as peak-to-peak voltage (Vpp), is shown in Fig. 5e and f for each PENG type. The presence of 30 wt% ZnO increases the output (from 233 ± 38 mV to 419 ± 24 mV, and from 1.83 ± 0.4 V to 2.72 ± 0.1 V for the type 1 and 2, respectively). Adding 0.5 wt % TrGO further enhances Vpp to 696 ± 52 mV and 3.22 ± 0.1 V for the respective PENG types. While ZnO increases generated currents (Fig. 5g and h), TrGO incorporation does not significantly affect the current regardless of PENG type. Fig. 5i and j demonstrate that increased voltage significantly boosts power densities of both PENG types, with notable increases after adding ZnO and TrGO. The type 2 PENG (with PDMS layer) achieves nearly tenfold higher power density for pure PCL and the ternary composite (30 wt% ZnO – 0.5 wt% TrGO) compared to the type 1, indicating optimal power output is achieved with additional triboelectric layers and conductive particles. Fig. 5k and l illustrate the voltage output of ternary PENGs composed of PCL with 30 wt% ZnO and 0.5 wt% TrGO when subjected to a 38 kHz, 560 W ultrasound bath, for both configurations. With the ultrasound off, only a few millivolts were detected, attributable to experimental noise. Upon activation, the voltage surged to over 100 mV peak-to-peak, regardless of configuration. This increase is attributed to the reduced triboelectric effect at higher frequencies due to shorter contact time between PENG layers, limiting electron flow; thus, the voltage arises mainly from the piezoelectric effect. Under ultrasound probe stimulation (1 MHz, 0.4 W/cm^2), which was used for cell stimulation, lower voltages up to 20 mV were observed for each configuration.

3.6. Preosteoblast cell culture

We cultured MC3T3-E1 mouse preosteoblasts on 3D-printed scaffolds to assess the biocompatibility of electroactive materials with and without ultrasound stimulation (1 MHz, 0.4 W/cm^2, 10 min daily). Fig. 6 shows confocal microscopy images of MC3T3-E1 cells on the scaffolds at day 14, with cell nuclei stained by DAPI (blue) and cytoskeleton by phalloidin Alexa 568 (red). Both non-stimulated and stimulated scaffolds exhibited cell adhesion and uniform distribution. Binary and ternary scaffolds with external stimulation had higher cell density, being a 15.1 %, 25.8 % and 36.0 % higher for Neat PCL, binary and ternary composites, respectively, and migration to porous regions where extracellular matrix (ECM) was deposited, acting as a physical barrier, anchorage site, and migration framework for cells [64]. In ternary scaffolds, pores were completely filled, indicating that piezoelectricity enhances cell spreading, consistent with previous observations in piezoelectric PLLA scaffolds modified with rGO and PDA [65]. This aligns with Angulo-Pineda et al., who found that 10 % TrGO in PCL scaffolds reduced hydrophobicity and enhanced cell adhesion [36]. The increased ECM synthesis and secretion may result from US stimulation upregulating certain transcription factors. For example, Ding et al. found that low-intensity pulsed ultrasound activated SOX9 in chondrocytes, promoting ECM secretion [66]. Additionally, US and piezoelectric materials activate mechanosensitive ion channels, including calcium and phosphate [67], crucial for ECM formation. Additionally, it can produce the activation of integrin-mediated mechanotransduction pathways, as well as thermal, cavitation, and standing wave phenomena which may be influencing focal adhesion kinase activation, crucial for cellular adhesion and propagation [68]. Further research is needed to clarify these findings. Zyrianova et al. recently developed a system with hydroxyapatite patterns and fiber-based biosensors to detect electrical signaling in cell communities without compromising cell integrity, potentially useful for studying ion release [69].

Fig. 7a illustrates the metabolic activity of cells within scaffolds over a 14-day culture period, confirming good biocompatibility for all scaffolds with and without ultrasound stimulation. Composite scaffolds showed slightly lower compatibility compared to PCL in non-stimulated conditions, likely due to higher local ZnO micro-rod concentrations affecting early cell adhesion [70]. However, binary and ternary scaffolds exhibited a significant increase in metabolic activity over time, unlike pure PCL scaffolds. Ultrasound stimulation did not significantly affect neat PCL scaffold metabolic activity during the 14-day culture, although a significant difference was observed for PCL scaffolds with 30 wt% ZnO. These findings suggest that while ultrasound improved cell proliferation in composites, as shown by confocal microscopy, it did not enhance metabolic activity measurements. This discrepancy may be attributed to factors such as frequency, intensity, and stimulation duration. High ultrasound frequencies, like those used in this study, are less effective at stimulating cells compared to lower frequencies due to wave attenuation [71]. Additionally, high ultrasound frequency reduces the effectiveness of the piezoelectric mechanism by lowering the polarization response and the effective voltage generated, thereby not promoting cell metabolic activity.

Total dsDNA concentration and ALP activity after 14 days of culture is presented in Fig. 7b and c. Under non-stimulated conditions, cell

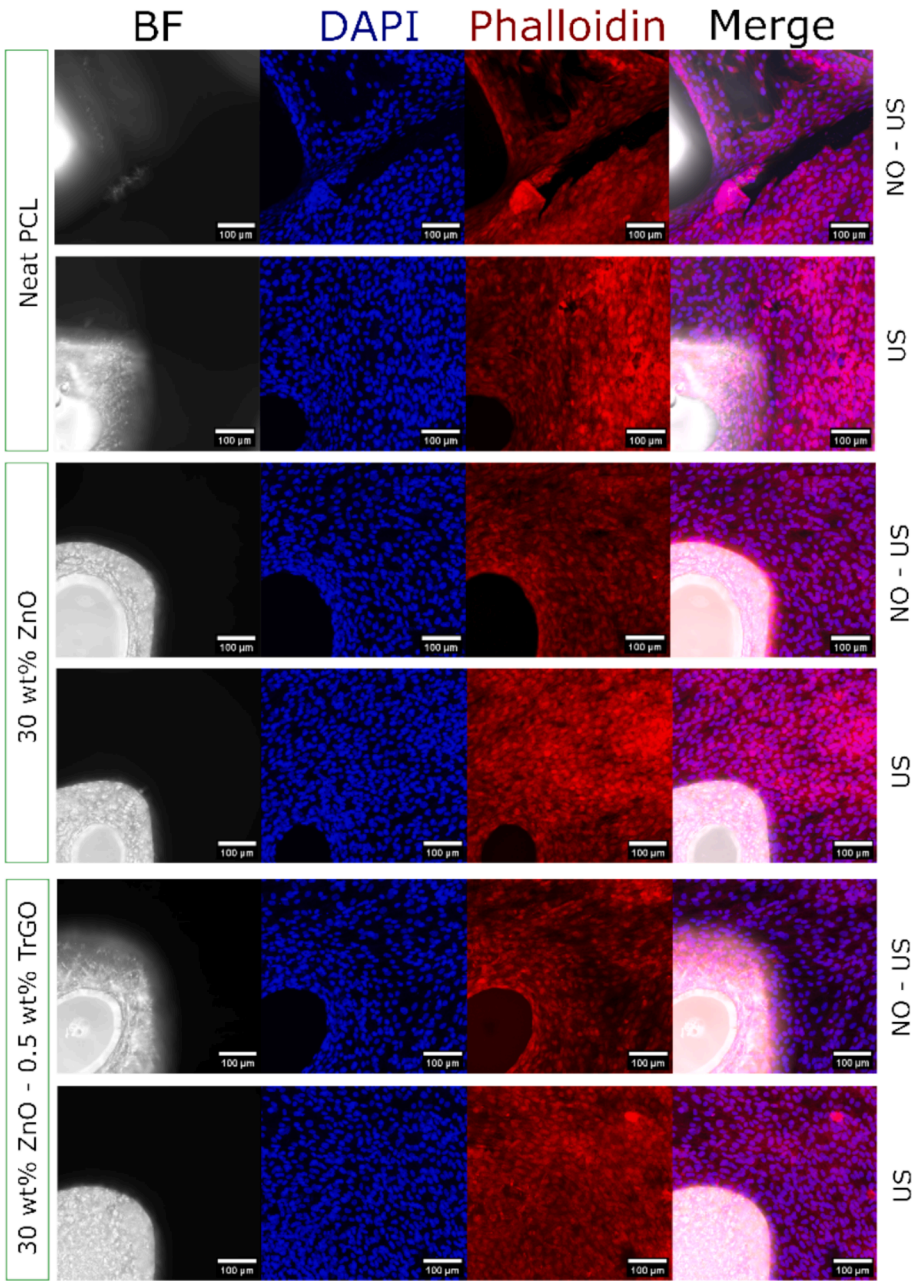

Fig. 6. Confocal microscopy images of 3D-printed scaffolds after 14-day culture. NO – US: no ultrasound stimulation; US: ultrasound stimulation.

density was similar across all scaffold compositions, indicating that ZnO and TrGO incorporation did not affect cell viability. Confocal microscopy showed enhanced cell response in US-stimulated scaffolds, but dsDNA measurements revealed no significant differences between groups. This discrepancy may be due to incomplete DNA extraction caused by the complex 3D-printed scaffold architecture, which can trap cellular components and interfere with cell lysis during extraction [72]. Optimizing steps like trypsinization and sonication for cell detachment could improve cell extraction from the 3D construct, allowing better comparison between microscopy and dsDNA assay results. Analysis of osteogenic differentiation showed that US stimulation significantly increased ALP activity in PCL scaffolds compared to non-stimulated counterparts, consistent with other studies using lower ultrasound intensities [73,74]. This effect may result from cavitation and mechanical stress, which alter cell permeability and promote the release of intracellular components such as ALP [75]. However, comparing ALP activity across different scaffold compositions under both US-stimulated and non-stimulated conditions revealed no significant differences. We hypothesize that the high US frequency used is insufficient to produce significant piezoelectric stimulation on cells. Although ZnO alone can upregulate ALP at transcriptional and protein levels [76], high concentrations of Zn^{+2} ions can inhibit its activity [77]. Consequently, the high ZnO particle concentration in binary and ternary scaffolds may diminish this boosting effect. Further studies on Zn^{+2} liberation into the media are needed to understand this phenomenon better.

4. Conclusions

We demonstrated that the 3D-printing process induced ZnO microrod alignment, dependent on particle concentration, as revealed by SEM, WAXS, and micro-CT. The aligned composites showed enhanced mechanical properties, including increased crystallinity, stiffness, and tensile and compressive strength. The addition of TrGO nanosheets further improved these properties, yielding mechanical characteristics

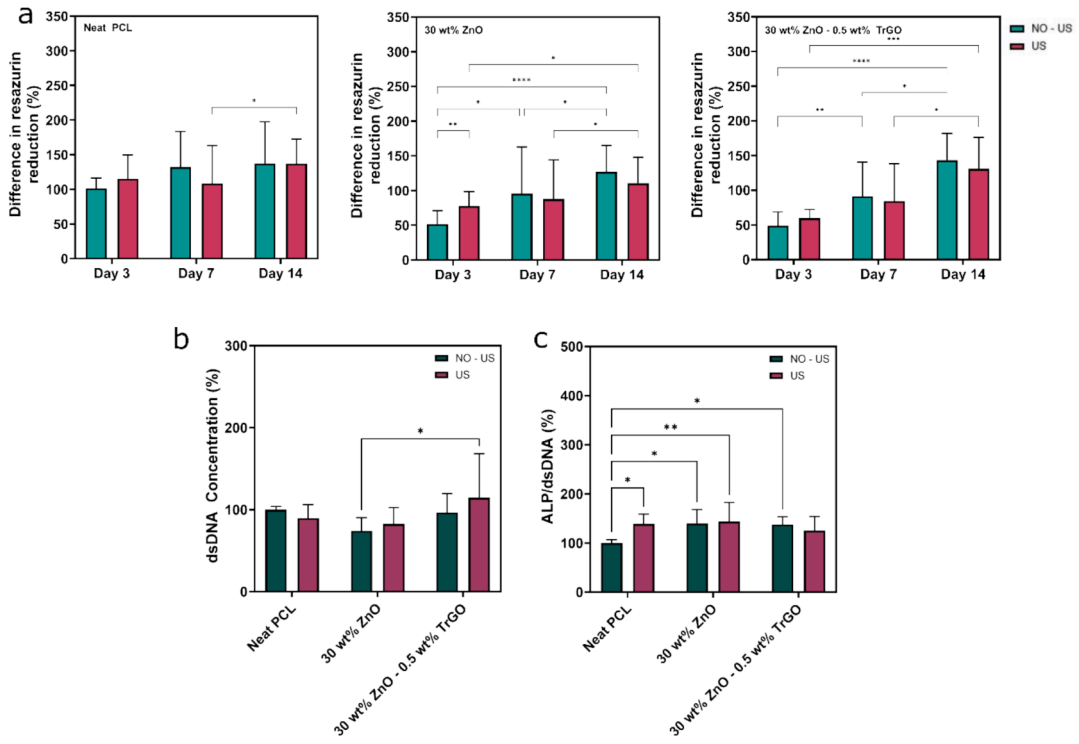

Fig. 7. A) Metabolic activity of MC3T3-E1 cells cultured in 3D-printed scaffolds for 3, 7, and 14 days under conditions of NO – US and US stimulation, obtained through the alamarBlue assay. b) dsDNA concentration of MC3T3-E1 cells on scaffolds after 14-day culture. c) Normalized ALP activity of MC3T3-E1 cells by dsDNA concentration on 3D-printed scaffolds after 14-day ns: not significant, *: $p < 0.05$, **: $p < 0.01$, ***: $p < 0.001$, ****: $p < 0.0001$.

similar to natural bone. The interaction between aligned ZnO micro-rods and TrGO nanosheets also enhanced relative permittivity and dielectric losses, resulting in superior piezoelectric performance at low conductive particle concentrations, comparable to native bone. Conductive particles facilitated charge collection and distribution in the insulating PCL matrix, enhancing voltage generation and supporting the proposed ZnO-TrGO synergy mechanism. Biological evaluation under ultrasound stimulation indicated that composite scaffolds had higher cell adhesion, biocompatibility, and promoted cell proliferation, migration, and ECM secretion. This work establishes a foundation for smart biomaterials with controlled microstructure and composition, enabling multifunctional scaffolds that promote tissue regeneration through mechanical and electrical cues, potentially improving outcomes in orthopedic and reconstructive surgery.

Declaration of Generative AI and AI-assisted technologies in the writing process

During the preparation of this work the author(s) used Paperpal in order to improve the writing and clarity of the writing. After using this tool/service, the author(s) reviewed and edited the content as needed and take(s) full responsibility for the content of the published article.

CRediT authorship contribution statement

Francisco Fernández-Gil: Writing – original draft, Visualization, Resources, Methodology, Investigation, Funding acquisition, Formal analysis, Data curation, Conceptualization. **Felipe Olate-Moya:** Writing – review & editing, Methodology, Investigation, Data curation. **José Ricardo Aguilar-Cosme:** Writing – review & editing, Methodology, Investigation. **Javier Garcia-Molleja:** Software, Investigation, Data curation. **Juan Pedro Fernández-Blázquez:** Writing – review & editing, Validation, Investigation, Formal analysis. **Sarah Cartmell:** Writing – review & editing, Supervision, Project administration, Funding acquisition. **Humberto Palza:** Writing – review & editing, Visualization, Validation, Supervision, Resources, Project administration, Funding acquisition, Conceptualization.

Funding

This work was supported by the National Doctoral Scholarship ANID No. 21210230, ANID-Basal Center of Interventional Medicine for Precision and Advanced Cellular Therapy, IMPACT, Project No. FB210024, ANID Exploration Project No. 13220007, and The Henry Royce Institute for Advanced Materials, UK (grant no. EP/R00661X/1, EP/S019367/1, EP/P025021/1, and EP/P025498/1).

Declaration of competing interest

The authors declare that they have no known competing financial interests or personal relationships that could have appeared to influence the work reported in this paper.

Acknowledgements

The authors acknowledge the National Doctoral Scholarship ANID No. 21210230, ANID Fondecyt Postdoctoral No. 3240135, ANID-Basal Center of Interventional Medicine for Precision and Advanced Cellular Therapy, IMPACT, Project No. FB210024, ANID Exploration Project No. 13220007, and The Henry Royce Institute for Advanced Materials (grant no. EP/R00661X/1, EP/S019367/1, EP/P025021/1, and EP/P025498/1), UK, for their support and equipment.

Appendix A. Supplementary data

Supplementary data to this article can be found online at https://doi.org/10.1016/j.matdes.2025.113672.

Data availability

Data will be made available on request.

References

[1] M.W. Archunan, S. Petronis, Bone grafts in trauma and orthopaedics, Cureus 13 (2021) 1–5, https://doi.org/10.7759/cureus.17705.

[2] S.S. Lee, X. Du, I. Kim, S.J. Ferguson, Scaffolds for bone-tissue engineering, Matter 5 (2022) 2722–2759, https://doi.org/10.1016/j.matt.2022.06.003.

[3] C. Jiao, D. Xie, Z. He, H. Liang, L. Shen, Y. Yang, et al., Additive manufacturing of bio-inspired ceramic bone scaffolds: structural design, mechanical properties and biocompatibility, Mater. Des. 217 (2022), https://doi.org/10.1016/j.matdes.2022.110610.

[4] T. Zhu, H. Zhou, X. Chen, Y. Zhu, Recent advances of responsive scaffolds in bone tissue engineering, Front. Bioeng. Biotechnol. 11 (2023), https://doi.org/10.3389/fbioe.2023.1296881.

[5] H. Wei, J. Cui, K. Lin, J. Xie, X. Wang, Recent advances in smart stimuli-responsive biomaterials for bone therapeutics and regeneration, Bone Res. 10 (2022) 17, https://doi.org/10.1038/s41413-021-00180-y.

[6] P. Sikder, P. Nagaraju, H.P.S. Naganaboyina, 3D-printed piezoelectric porous bioactive scaffolds and clinical ultrasonic stimulation can help in enhanced bone regeneration, Bioengineering 9 (2022), https://doi.org/10.3390/bioengineering9110679.

[7] C. Polley, T. Distler, C. Scheufler, R. Detsch, H. Lund, A. Springer, et al., 3D printing of piezoelectric and bioactive barium titanate-bioactive glass scaffolds for bone tissue engineering, Mater. Today Bio 21 (2023), https://doi.org/10.1016/j.mtbio.2023.100719.

[8] B.I. Oladapo, S.O. Ismail, J.F. Kayode, O.M. Ikumapayi, Piezoelectric effects on bone modeling for enhanced sustainability, Mater. Chem. Phys. 305 (2023), https://doi.org/10.1016/j.matchemphys.2023.127960.

[9] R. Das, D. Le, H.M. Kan, T.T. Le, J. Park, T.D. Nguyen, et al., Osteo-inductive effect of piezoelectric stimulation from the poly(l-lactic acid) scaffolds, PLoS One 19 (2024), https://doi.org/10.1371/journal.pone.0299579.

[10] M.J. Javid-Naderi, J. Behravan, N. Karimi-Hajishohreh, S. Toosi, Synthetic polymers as bone engineering scaffold, Polym. Adv. Technol. 34 (2023) 2083–2096, https://doi.org/10.1002/pat.6046.

[11] R. Donate, R. Paz, R. Moriche, M.J. Sayagués, M.E. Alemán-Domínguez, M. Monzón, An overview of polymeric composite scaffolds with piezoelectric properties for improved bone regeneration, Mater. Des. 231 (2023), https://doi.org/10.1016/j.matdes.2023.112085.

[12] K.S. Ramadan, D. Sameoto, S. Evoy, A review of piezoelectric polymers as functional materials for electromechanical transducers, Smart Mater. Struct. 23 (2014), https://doi.org/10.1088/0964-1726/23/3/033001.

[13] E. Mystiridou, A.C. Patsidis, N. Bouropoulos, Development and characterization of 3D printed multifunctional bioscaffolds based on PLA/PCL/HAp/BaTiO3 composites, Appl. Sci. (Switzerland) 11 (2021), https://doi.org/10.3390/app11094253.

[14] X. Dai, X. Yao, W. Zhang, H. Cui, Y. Ren, J. Deng, et al., The osteogenic role of barium titanate/polylactic acid piezoelectric composite membranes as guiding membranes for bone tissue regeneration, Int. J. Nanomed. 17 (2022) 4339–4353, https://doi.org/10.2147/IJN.S378422.

[15] F. Owusu, T.R. Venkatesan, F.A. Nüesch, R.M. Negri, D.M. Opris, How to make elastomers piezoelectric? Adv. Mater. Technol. 8 (2023) https://doi.org/10.1002/admt.202300099.

[16] V.L. Stuber, T.R. Mahon, S. van der Zwaag, P. Groen, The effect of the intrinsic electrical matrix conductivity on the piezoelectric charge constant of piezoelectric composites, Mater. Res. Express 7 (2020) 015703, https://doi.org/10.1088/2053-1591/ab5bb3.

[17] Y. Yan, L.D. Geng, H. Liu, H. Leng, X. Li, Y.U. Wang, et al., Near-ideal electromechanical coupling in textured piezoelectric ceramics, Nat. Commun. 13 (2022), https://doi.org/10.1038/s41467-022-31165-y.

[18] G. Tian, W. Deng, D. Xiong, T. Yang, B. Zhang, X. Ren, et al., Dielectric micro-capacitance for enhancing piezoelectricity via aligning MXene sheets in composites, Cell Rep. Phys. Sci. 3 (2022) 100814, https://doi.org/10.1016/j.xcrp.2022.100814.

[19] J. Fan, N. Deneke, S. Xu, B. Newell, J. Garcia, C. Davis, et al., Electric poling-assisted additive manufacturing technique for piezoelectric active poly(vinylidene fluoride) films: Towards fully three-dimensional printed functional materials, Addit. Manuf. 60 (2022), https://doi.org/10.1016/j.addma.2022.103248.

[20] G. Tselikos, S. Rasul, P. Groen, C. Li, J. Khaliq, In situ printing and functionalization of hybrid polymer-ceramic composites using a commercial 3d printer and dielectrophoresis—a novel conceptual design, Polymers (basel) 13 (2021), https://doi.org/10.3390/polym13223979.

[21] W. Xu, S. Jambhulkar, D. Ravichandran, Y. Zhu, M. Kakarla, Q. Nian, et al., 3D printing-enabled nanoparticle alignment: a review of mechanisms and applications, Small 17 (2021), https://doi.org/10.1002/smll.202100817.

[22] H. Tang, Y. Lin, H.A. Sodano, Enhanced energy storage in nanocomposite capacitors through aligned PZT nanowires by uniaxial strain assembly, Adv. Energy Mater. 2 (2012) 469–476, https://doi.org/10.1002/aenm.201100543.

[23] X. Zhang, M.Q. Le, O. Zahhaf, J.F. Capsal, P.J. Cottinet, L. Petit, Enhancing dielectric and piezoelectric properties of micro-ZnO/PDMS composite-based dielectrophoresis, Mater. Des. 192 (2020), https://doi.org/10.1016/j.matdes.2020.108783.

[24] J. Long, W. Xiong, C. Wei, C. Lu, R. Wang, C. Deng, et al., Directional assembly of ZnO nanowires via three-dimensional laser direct writing, Nano Lett. 20 (2020) 5159–5166, https://doi.org/10.1021/acs.nanolett.0c01378.

[25] Z. Huan, H.K. Chu, H. Liu, J. Yang, D. Sun, Engineered bone scaffolds with dielectrophoresis-based patterning using 3D printing, Biomed. Microdevices 19 (2017), https://doi.org/10.1007/s10544-017-0245-5.

[26] M.H. Malakooti, F. Julé, H.A. Sodano, Printed nanocomposite energy harvesters with controlled alignment of barium titanate nanowires, ACS Appl. Mater. Interfaces 10 (2018) 38359–38367, https://doi.org/10.1021/acsami.8b13643.

[27] A. Renteria, L.F. Garcia, V.H. Balcorta, D. Ortiz, L.C. Delfin, J. Regis, et al., Influence of bimodal particle distribution on material properties of BaTiO3 fabricated by paste extrusion 3D printing, Ceram. Int. 47 (2021) 18477–18486, https://doi.org/10.1016/j.ceramint.2021.03.171.

[28] C. Li, G. Chen, X. Qiu, Q. Lou, X. Gao, A direct proof for Maxwell-Wagner effect of heterogeneous interface, AIP Adv. 11 (2021), https://doi.org/10.1063/5.0040947.

[29] B. Li, C.A. Randall, E. Manias, Polarization mechanism underlying strongly enhanced dielectric permittivity in polymer composites with conductive fillers, J. Phys. Chem. C 126 (2022) 7596–7604, https://doi.org/10.1021/acs.jpcc.2c01592.

[30] X. Xia, Z. Zhong, G.J. Weng, Maxwell–Wagner–Sillars mechanism in the frequency dependence of electrical conductivity and dielectric permittivity of graphene-polymer nanocomposites, Mech. Mater. 109 (2017) 42–50, https://doi.org/10.1016/j.mechmat.2017.03.014.

[31] Y. Jin, N. Chen, Y. Li, Q. Wang, The selective laser sintering of a polyamide 11/BaTiO3/graphene ternary piezoelectric nanocomposite, RSC Adv. 10 (2020) 20405–20413, https://doi.org/10.1039/d0ra01042a.

[32] F. Qi, N. Chen, Q. Wang, Dielectric and piezoelectric properties in selective laser sintered polyamide11/BaTiO3/CNT ternary nanocomposites, Mater. Des. 143 (2018) 72–80, https://doi.org/10.1016/j.matdes.2018.01.050.

[33] S. Mamada, N. Yaguchi, M. Hansaka, M. Yamato, H. Yoshida, Matrix influence on the piezoelectric properties of piezoelectric ceramic/polymer composite exhibiting particle alignment, J. Appl. Polym. Sci. 132 (2015), https://doi.org/10.1002/app.41817.

[34] F.C.M. Freire Filho, J.A. Santos, A.O. Sanches, E.S. Medeiros, J.A. Malmonge, M. J. Silva, Dielectric, electric, and piezoelectric properties of three-phase piezoelectric composite based on castor-oil polyurethane, lead zirconate titanate particles and multiwall carbon nanotubes, J. Appl. Polym. Sci. 140 (2023), https://doi.org/10.1002/app.53572.

[35] D.A. Triana-Camacho, O.A. Mendoza Reales, J.H. Quintero-Orozco, Low concentrations of gold nanoparticles as electric charge carriers in piezoelectric cement-based materials, Materials 17 (2024), https://doi.org/10.3390/ma17030615.

[36] C. Angulo-Pineda, K. Srirussamee, P. Palma, V.M. Fuenzalida, S.H. Cartmell, H. Palza, Electroactive 3D printed scaffolds based on percolated composites of polycaprolactone with thermally reduced graphene oxide for antibacterial and tissue engineering applications, Nanomaterials 10 (2020) 428, https://doi.org/10.3390/nano10030428.

[37] N. Peidavosi, M. Azami, N. Beheshtizadeh, S.A. Ramazani, Piezoelectric conductive electrospun nanocomposite PCL/Polyaniline/Barium Titanate scaffold for tissue engineering applications, Sci. Rep. 12 (2022), https://doi.org/10.1038/s41598-022-25332-w.

[38] C.R. Chandraiahgari, G. De Bellis, P. Ballirano, S.K. Balijepalli, S. Kaciulis, L. Caneve, et al., Synthesis and characterization of ZnO nanorods with a narrow size distribution, RSC Adv. 5 (2015) 49861–49870, https://doi.org/10.1039/C5RA02631H.

[39] S. Mustapha, M.M. Ndamitso, A.S. Abdulkareem, J.O. Tijani, D.T. Shuaib, A. K. Mohammed, et al., Comparative study of crystallite size using Williamson-Hall and Debye-Scherrer plots for ZnO nanoparticles, Adv. Nat. Sci. 10 (2019) 5, https://doi.org/10.1088/2043-6254/ab52f7.

[40] Z. Uddin, M.J. Uddin, M.R. Islam, M.S. Alam, T. Soga, M.S.H. Choudhury, Estimation of ZnO nanoparticles crystallite parameters at different compression temperatures, in: 2021 5th International Conference on Electrical Engineering and Information and Communication Technology, ICEEICT 2021, Institute of Electrical and Electronics Engineers Inc., 2021, https://doi.org/10.1109/ICEEICT53905.2021.9667845.

[41] D. Kaur, A. Bharti, T. Sharma, C. Madhu, Dielectric properties of ZnO-based nanocomposites and their potential applications, Int. J. Opt. 2021 (2021) 1–20, https://doi.org/10.1155/2021/9950202.

[42] R. Arul, R.N. Oosterbeek, J. Robertson, G. Xu, J. Jin, M.C. Simpson, The mechanism of direct laser writing of graphene features into graphene oxide films involves photoreduction and thermally assisted structural rearrangement, Carbon N. Y. 99 (2016) 423–431, https://doi.org/10.1016/j.carbon.2015.12.038.

[43] G. Wei, J. Yu, M. Gu, T.B. Tang, Dielectric relaxation and hopping conduction in reduced graphite oxide, J. Appl. Phys. 119 (2016), https://doi.org/10.1063/1.4953357.

[44] A. Saranya, T. Devasena, H. Sivaram, R. Jayavel, Role of hexamine in ZnO morphologies at different growth temperature with potential application in dye sensitized solar cell, Mater. Sci. Semicond. Process. 92 (2019) 108–115, https://doi.org/10.1016/j.mssp.2018.03.028.

[45] H.M. Schrickx, P. Sen, N. Balar, B.T. O'Connor, Strain alignment of conjugated polymers: Method, microstructure, and applications, Cell Rep. Phys. Sci. 5 (2024), https://doi.org/10.1016/j.xcrp.2024.102076.

[46] H.S. Varol, F. Meng, B. Hosseinkhani, C. Malm, D. Bonn, M. Bonn, et al., Nanoparticle amount, and not size, determines chain alignment and nonlinear hardening in polymer nanocomposites, PNAS 114 (2017) E3170–E3177, https://doi.org/10.1073/pnas.1617069114.

[47] A. Ben Abdallah, A. Kallel, F. Gamaoun, A. Tcharkhtchi, Enzymatic Hydrolysis of Poly (Caprolactone) and its Blend with Styrene–Butadiene–Styrene (40% PCL/60% SBS), J. Polym. Environ. 27 (2019) 2341–2351, https://doi.org/10.1007/s10924-019-01522-y.
[48] S. Huan, G. Liu, W. Cheng, G. Han, L. Bai, Electrospun poly(lactic acid)-based fibrous nanocomposite reinforced by cellulose nanocrystals: impact of fiber uniaxial alignment on microstructure and mechanical properties, Biomacromolecules 19 (2018) 1037–1046, https://doi.org/10.1021/acs.biomac.8b00023.
[49] E. Tarani, I. Arvanitidis, D. Christofilos, D.N. Bikiaris, K. Chrissafis, G. Vourlias, Calculation of the degree of crystallinity of HDPE/GNPs nanocomposites by using various experimental techniques: a comparative study, J. Mater. Sci 58 (2023) 1621–1639, https://doi.org/10.1007/s10853-022-08125-4.
[50] R. Augustine, N. Kalarikkal, S. Thomas, Effect of zinc oxide nanoparticles on the in vitro degradation of electrospun polycaprolactone membranes in simulated body fluid, Int. J. Polym. Mater. Polym. Biomater. 65 (2016) 28–37, https://doi.org/10.1080/00914037.2015.1055628.
[51] J.J. Martin, M.S. Riederer, M.D. Krebs, R.M. Erb, Understanding and overcoming shear alignment of fibers during extrusion, Soft Matter 11 (2015) 400–405, https://doi.org/10.1039/c4sm02108h.
[52] P. Consul, K.U. Beuerlein, G. Luzha, K. Drechsler, Effect of extrusion parameters on short fiber alignment in fused filament fabrication, Polymers (basel) 13 (2021), https://doi.org/10.3390/polym13152443.
[53] X. Wu, X. Chen, S. Li, K. Li, W. Gu, Jet diameter dependence on nozzle size in DC-driven electrohydrodynamics printing, Eng. Res. Express 1 (2019), https://doi.org/10.1088/2631-8695/ab54a3.
[54] E. Bertevas, J. Férec, B.C. Khoo, G. Ausias, N. Phan-Thien, Smoothed particle hydrodynamics (SPH) modeling of fiber orientation in a 3D printing process, Phys. Fluids 30 (2018), https://doi.org/10.1063/1.5047088.
[55] M.K. Hausmann, P.A. Rühs, G. Siqueira, J. Läuger, R. Libanori, T. Zimmermann, et al., Dynamics of cellulose nanocrystal alignment during 3D printing, ACS Nano 12 (2018) 6926–6937, https://doi.org/10.1021/acsnano.8b02366.
[56] S. Oh, R. Hayakawa, C. Pan, K. Sugiyasu, Y. Wakayama, Polymer chain alignment and transistor properties of nanochannel-templated poly(3-hexylthiophene) nanowires, J. Appl. Phys. 120 (2016), https://doi.org/10.1063/1.4960133.
[57] P. Haji Mohammadi Gohari, M. Haghbin Nazarpak, M. Solati-Hashjin, The effect of adding reduced graphene oxide to electrospun polycaprolactone scaffolds on MG-63 cells activity, Mater. Today Commun. 27 (2021) 102287, https://doi.org/10.1016/j.mtcomm.2021.102287.
[58] H.J. Mao, D.F. Liu, N. Zhang, T. Huang, I. Kühnert, J.H. Yang, et al., Constructing a microcapacitor network of carbon nanotubes in polymer blends via crystallization-induced phase separation toward high dielectric constant and low loss, ACS Appl Mater Interfaces 12 (2020) 26444–26454, https://doi.org/10.1021/acsami.0c04575.
[59] S. Román, F. Lund, J. Bustos, H. Palza, About the relevance of waviness, agglomeration, and strain on the electrical behavior of polymer composites filled with carbon nanotubes evaluated by a Monte-Carlo simulation, Mater. Res. Express 5 (2018), https://doi.org/10.1088/2053-1591/aaa531.
[60] J. Liu, H. Gu, Q. Liu, L. Ren, G. Li, An intelligent material for tissue reconstruction: The piezoelectric property of polycaprolactone/barium titanate composites, Mater. Lett. 236 (2019) 686–689, https://doi.org/10.1016/j.matlet.2018.11.036.
[61] A. Morali, A. Mandal, M. Skorobogatiy, S. Bodkhe, Unleashing the piezoelectric potential of PVDF: a study on phase transformation from gamma (γ) to beta (β) phase through thermal contact poling, RSC Adv. 13 (2023) 31234–31242, https://doi.org/10.1039/d3ra05068h.
[62] Y. Ting, N.A. Suprapto, C.W. Chiu, H. Gunawan, Design and characterization of one-layer PVDF thin film for a 3D force sensor, Sens. Actuators A Phys. 250 (2016) 129–137, https://doi.org/10.1016/j.sna.2016.09.025.
[63] R. Joshi, I. Lahiri, Working Principles and Mechanisms in Nanogenerators. Nanogenerators, CRC Press (2022) 17–32, https://doi.org/10.1201/9781003187615-2.
[64] B. Yue, Biology of the extracellular matrix: an overview, J. Glaucoma 23 (2014) S20–S23, https://doi.org/10.1097/IJG.0000000000000108.
[65] Y.H. Lai, Y.H. Chen, A. Pal, S.H. Chou, S.J. Chang, E.W. Huang, et al., Regulation of cell differentiation via synergistic self-powered stimulation and degradation behavior of a biodegradable composite piezoelectric scaffold for cartilage tissue, Nano Energy 90 (2021), https://doi.org/10.1016/j.nanoen.2021.106545.
[66] W. Ding, D. Du, S. Chen, LIPUS promotes synthesis and secretion of extracellular matrix and reduces cell apoptosis in human osteoarthritis through upregulation of SOX9 expression, Int. J. Clin Exp. Pathol. 13 (2020) 810–817.
[67] X. Hou, L. Liu, L. Sun, Precise modulation of cell activity using sono-responsive nano-transducers, Biomaterials 314 (2025), https://doi.org/10.1016/j.biomaterials.2024.122857.
[68] K.W. Jang, L. Ding, D. Seol, T.H. Lim, J.A. Buckwalter, J.A. Martin, Low-Intensity pulsed ultrasound promotes chondrogenic progenitor cell migration via focal adhesion kinase pathway, Ultrasound Med. Biol. 40 (2014) 1177–1186, https://doi.org/10.1016/j.ultrasmedbio.2013.12.007.
[69] P.I. Zyrianova, M.M. Eltantawy, D.V. Silin, I.S. Korolev, K.G. Nikolaev, D. A. Kozodaev, et al., Biomimetic materials based on hydroxyapatite patterns for studying extracellular cell communication, Mater. Des. 238 (2024), https://doi.org/10.1016/j.matdes.2024.112718.
[70] J.T. Seil, T.J. Webster, Decreased astroglial cell adhesion and proliferation on zinc oxide nanoparticle polyurethane composites, vol. 3, 2008.
[71] T. Riis, J. Kubanek, Effective ultrasonic stimulation in human peripheral nervous system, IEEE Trans. Biomed. Eng. 69 (2022) 15–22, https://doi.org/10.1109/TBME.2021.3085170.
[72] S.C. Santos, C.A. Custódio, J.F. Mano, Human protein-based porous scaffolds as platforms for xeno-free 3D cell culture, Adv. Healthc. Mater. 11 (2022), https://doi.org/10.1002/adhm.202102383.
[73] W.M. Maung, H. Nakata, M. Miura, M. Miyasaka, Y.K. Kim, S. Kasugai, et al., Low-intensity pulsed ultrasound stimulates osteogenic differentiation of periosteal cells in vitro, Tissue Eng. Part A 27 (2021) 63–73, https://doi.org/10.1089/ten.tea.2019.0331.
[74] B. Hu, Y. Zhang, J. Zhou, J. Li, F. Deng, Z. Wang, et al., Low-intensity pulsed ultrasound stimulation facilitates osteogenic differentiation of human periodontal ligament cells, PLoS One 9 (2014) e95168, https://doi.org/10.1371/journal.pone.0095168.
[75] S. Qin, C. Hu, O. Oenema, Differentiating intracellular from extracellular alkaline phosphatase activity in soil by sonication, PLoS One 8 (2013), https://doi.org/10.1371/journal.pone.0058691.
[76] M. Pandurangan, D.H. Kim, ZnO nanoparticles augment ALT, AST, ALP and LDH expressions in C2C12 cells, Saudi J. Biol. Sci. 22 (2015) 679–684, https://doi.org/10.1016/j.sjbs.2015.03.013.
[77] Y.H. Chu, X.X. Yu, X. Jin, Y.T. Wang, D.J. Zhao, P. Zhang, et al., Purification and characterization of alkaline phosphatase from lactic acid bacteria, RSC Adv. 9 (2019) 354–360, https://doi.org/10.1039/C8RA08921C.